Scale dependence of bubble creation mechanisms in breaking waves

Grant B. Deane & M. Dale Stokes

Marine Physical Laboratory, Scripps Institution of Oceanography, University of California at San Diego, La Jolla, California 92093-0238, USA

Breaking ocean waves entrain air bubbles that enhance air–sea gas flux, produce aerosols, generate ambient noise and scavenge biological surfactants. The size distribution of the entrained bubbles is the most important factor in controlling these processes, but little is known about bubble properties and formation mechanisms inside whitecaps. We have measured bubble size distributions inside breaking waves in the laboratory and in the open ocean, and provide a quantitative description of bubble formation mechanisms in the laboratory. We find two distinct mechanisms controlling the size distribution, depending on bubble size. For bubbles larger than about 1 mm, turbulent fragmentation determines bubble size distribution, resulting in a bubble density proportional to the bubble radius to the power of −10/3. Smaller bubbles are created by jet and drop impact on the wave face, with a −3/2 power-law scaling. The length scale separating these processes is the scale where turbulent fragmentation ceases, also known as the Hinze scale. Our results will have important implications for the study of air–sea gas transfer.

Breaking waves in the open ocean create dense plumes of bubbles that can extend 0.5 m or more below the surface and have void fractions of air exceeding 10%. The bubbles in the plumes range in size from tens of micrometres to centimetres, and are known to be important for a number of diverse phenomena, including the enhanced transport of gases across the ocean surface, ambient noise generation, the production of aerosols, and the scavenging of biological surfactants[1–4]. The single most important property of the bubbles is their size distribution. The distributions and dynamics of bubbles in the upper ocean tens to hundreds of seconds after their formation are fairly well understood[5–11]. But few field measurements have been made of bubbles during the first seconds of wave breaking[12–15] and within the high-void-fraction region of the whitecap, and bubble formation mechanisms have not been quantified. One of the problems with existing measurements of oceanic bubble size distributions is that the bubble spectrum evolves quite rapidly in the first second or so after the active phase of air entrainment ceases, making it difficult to reconcile different data sets without knowing the exact age of the bubble plume. This rapid evolution has been described by Monahan[8], who introduced the idea of dense 'alpha' and more diffuse 'beta' plumes.

Models of breaking-wave bubble spectra have been proposed. Longuet-Higgins[16] considered the bubble size spectrum created by the random cleaving of a cube, and showed that, as the number of cleaving events becomes large, the resulting bubble distributions resemble that of observations. However, this theory does not offer a way of relating the size distribution to the physical properties of the wave. Baldy[17] discussed bubble formation under the assumption that the bubble creation rate depends only on ε, the fluid turbulent dissipation rate, and the bubble formation energy, resulting in a -2 power-law scaling with radius. Garrett *et al.*[18] have proposed a cascade of bubble fragmentation events with the bubble spectrum depending only on ε and the average rate of supply of air, resulting in a $-10/3$ power-law scaling. In addition, there has been significant work on bubble splitting in sheared and turbulent flows and air entrainment by plunging jets and drops (see, for example, refs 19–21).

However, there are no prior observations of bubble formation processes inside breaking waves. Photographic studies of air entrainment in laboratory waves have been reported previously[22–24], but at insufficient temporal and spatial scales to resolve bubble formation mechanisms within the breaking crest. The problem is making measurements on the appropriate length and time scales in the complex two-phase flow inside a breaking wave. Using optical and acoustical observations of bubble formation, we have quantified various aspects of the phenomena determining the bubble size spectrum in laboratory and oceanic waves.

The origin of the bubble size spectrum

The lifetime of wave-generated bubbles falls into two phases. The first phase occurs as bubbles are entrained and fragmented inside the breaking wave crest. Newly created bubbles produce pulses of sound, so this period is accompanied by a burst of noise and we refer to it as the acoustically active phase. Once bubble creation processes cease, the newly formed bubble plume becomes acoustically quiescent and evolves under the influence of turbulent diffusion, advection, buoyant degassing and dissolution. In Monahan's[8] nomenclature, both these phases fall within the lifetime of an

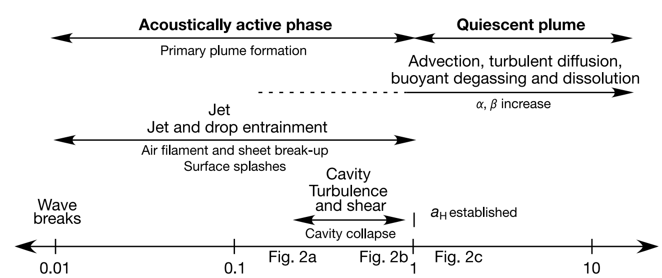

Figure 1 Logarithmic timeline of bubble plume evolution. Plume lifetime can be divided into two main phases—the acoustic phase when bubbles are formed, and the quiescent phase which begins when active bubble formation ceases. The physical processes occurring during the acoustic phase determine the initial bubble size distribution. The quiescent plume evolves rapidly under the influence of buoyant degassing, turbulent diffusion, advection and dissolution. Most oceanic bubble size distributions have been measured in quiescent plumes which have evolved from the initial size distribution. Two primary mechanisms determine the bubble size distribution during the acoustic phase. The first is jet and drop entrainment, which is active during the entire acoustic phase and determines the slope (α) of the size distribution for bubbles smaller than the Hinze scale (a_H). The second is bubble fragmentation in turbulent and sheared flow. This mechanism operates during the wave cavity collapse, and determines the slope (β) of the distribution for bubbles larger than the Hinze scale. The Hinze scale is determined by the turbulent dissipation rate within the breaking wave crest. Labels on the time axis show when the images of plume formation were taken (Fig. 2).

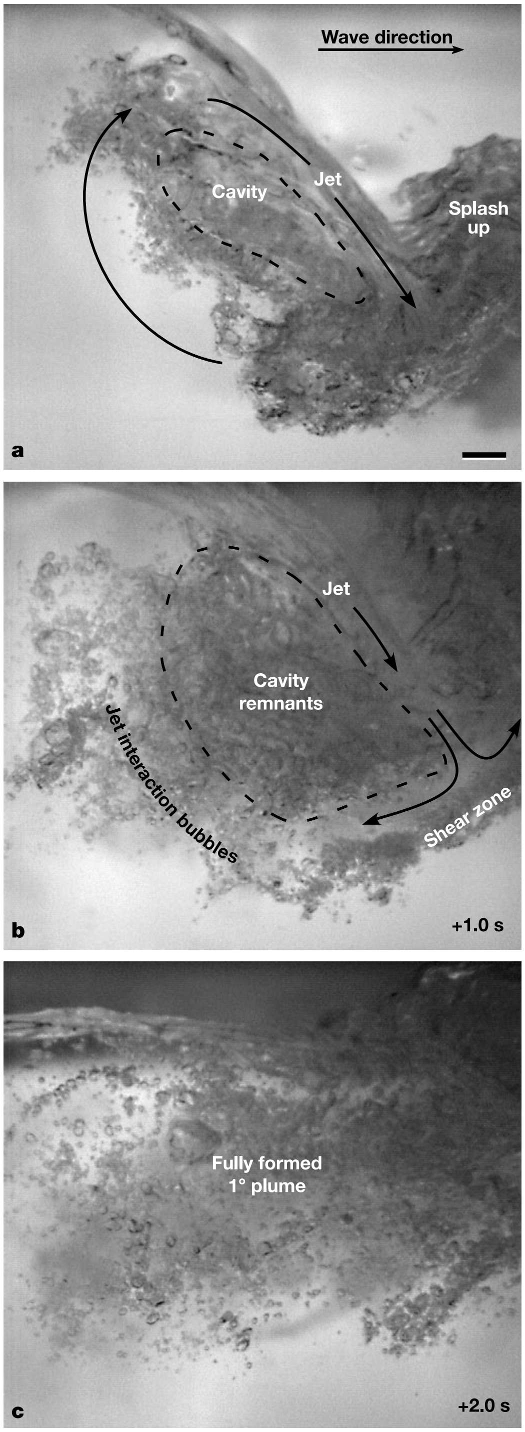

Figure 2 Three high-speed video images of a breaking wave crest taken during the acoustically active phase of the wave crest. Scale bar in **a**, 1 cm. The air–water boundaries scatter light out of the plane of illumination and appear darker. **a**, Bubble formation before the cavity of air trapped between the overturning jet and the wave face has fragmented. The bubbles around the lower half of the cavity were formed by jet and drop impact at the wave face and then advected around the cavity by clockwise flow. **b**, Bubble formation during the collapse of the air cavity. The jet-induced bubbles encircle the cavity remnants, and the jet/wave-face interaction region has developed into a shear zone. Detailed image analysis shows that bubble fragmentation occurs both inside the cavity region and in the shear zone. **c**, Bubble plume at the end of the acoustic phase. Image sequences were captured at 250 or 1,000 frames s^{-1} and a shutter speed of 1/3,000 s using a Kodak Motioncorder SR-1000 camera.

alpha plume. Here we describe the physical processes that control bubble formation during the active phase, and determine the bubble spectrum at the transition between the acoustically active and quiescent plumes. These phases are delineated in Fig. 1, which shows a logarithmic timeline annotated with the various processes dominating bubble evolution.

We conducted a series of experiments in a seawater wave flume (33 m long, 0.5 m wide, 0.6 m water depth). Wave packets were generated at one end of the flume using a computer-controlled wave paddle, which produced plunging breakers approximately 10 cm in height. The amplitude and phase of the wave-packet frequency components were generated so that they added constructively at the wave break point, producing a breaking wave. The wave-packet centre frequency, wavelength, relative bandwidth and slope were respectively 0.73 Hz, 2.3 m, 1 and 0.4. Surface elevation time series computed from pressure measurements made upstream and downstream of the breaking region were used to compute the wave-packet energy lost owing to breaking, and to ensure that events were repeatable. Events were imaged a few centimetres (2.5–18 cm) away from the glass-walled side of the flume using a high-speed video camera and front and back lighting. Simultaneous measurements of the noise generated by the wave crest were made with a hydrophone beneath the breaking region.

The breaking wave crest produces a complicated two-phase flow that evolves over a range of length and time scales. Those flow features that form distinct and repeatable patterns are shown in Fig. 2. Figure 2a shows the flow after the overturning wave crest (plunging jet) has struck the wave face, but before the cavity of air trapped between the jet and wave face (cavity) has fragmented. The arrows indicate the clockwise circulation around the cavity caused by the wave motion. The impact of the jet on the wave face causes a reactionary splash-up, which results in the formation of a secondary bubble plume. Figure 2b shows the same wave crest 1 s later. The cavity has almost completely fragmented, and the plunging jet has formed a shear layer on the wave face. Sometimes a layer of air trapped between the spreading jet and wave face is observed to form and split into filaments and bubbles. The cavity remnants are encircled by a cloud of bubbles formed by the interaction of the plunging jet with the wave face. The clockwise circulation around the cavity advects bubbles entrained by the jet and, ultimately, some of them are re-circulated through the jet. Figure 2c shows the wave crest 2 s later. The plunging jet has collapsed, leaving a fully formed, quiescent plume of bubbles.

The images in Fig. 2 suggest two distinct flow features driving bubble creation: the jet/wave-face interaction and the collapsing cavity. This view is supported by an analysis of the underwater noise radiated by the breaking wave. Newly created bubbles act like damped resonators and emit a pulse of sound[25,26]. The centre frequency of the sound pulse varies inversely with bubble radius (for example, a 3.3-mm-radius bubble resonates at approximately 1 kHz near the sea surface), so the breaking-wave noise is characteristic of the sizes of bubbles being created within the crest and persists while bubbles are being formed. Figure 3 shows a spectrogram of wave noise averaged over 17 breaking events and plotted as a colour contour map versus frequency and time. The acoustic frequency (F) expressed in terms of a resonant bubble radius (a) are shown on the left-hand side of the figure. The flow structures characteristic of different phases of noise emission are shown in images at the bottom of the figure.

Two distinct periods of sound production can be seen in the spectrogram. The period labelled 'Jet' is associated with the creation of bubbles from 2 mm down to at least 0.1 mm radius, and persists through the entire acoustically active phase. The shorter period, labelled 'Cavity', contains a burst of low-frequency noise centred around 300 Hz, and is associated with the creation of much larger bubbles (2 mm to $\geq$10 mm radius). Examination of video images shows that this noise is simultaneous with the breakup of the cavity.

The low-frequency sound generated by the cavity breakup is not radiated before its collapse, implying that bubbles larger than about 2 mm are produced only during cavity collapse. This is confirmed by manual, optical bubble counts taken before and during cavity collapse (not shown).

One of the primary objectives of this study was to measure the bubble size distribution within the interior of actively breaking wave crests. This has been accomplished by manually identifying and sizing bubbles in images similar to those shown in Fig. 2. Because the bubble size spectra are calculated from two-dimensional images of a three-dimensional volume, the size distribution estimates can be biased by bubble occlusion and bisection of large bubbles by the image plane. However, when the thickness of the sample section is small relative to the total area of the image, the biases are negligible[27].

Figure 4 shows the result of the image analysis. The bubble size distribution was estimated from approximately 225 images taken during the acoustically active period of 14 wave-breaking events. The bubble spectrum shows two distinct scaling laws (with power-law exponents α and β respectively) with a break point at slightly less than 1 mm. The power-law scaling of bubble density on radius is $-3/2$ for bubbles smaller than about 1 mm and $-10/3$ for larger bubbles. Figure 4 inset shows the temporal evolution of bubbles observed in a single plume. The upper curve was measured at the transition between the active and quiescent phases, and it shows the same power-law scaling as the ensemble average. The lower curve was measured 1.5 s later, and both α and β show a significant increase due to bubble degassing and dissolution. This illustrates the rapid evolution of the bubble spectrum once active bubble creation processes have stopped, and provides a context for interpreting oceanic bubble spectra where the age of the plume is often uncertain.

Bubble breakup in turbulent and sheared flow

The density of bubbles larger than about 1 mm follows a $-10/3$ power-law scaling with radius. The acoustic data and visual observation of cleaving bubbles suggest that these bubbles are created as the air cavity fragments[24] and bubbles split in the shear zone. Garrett *et al.*[18] envisage a physical process where air is entrained into relatively large bubbles, which fragment into smaller bubbles at a rate which depends on ε. Assuming that the bubble size spectrum $N(a)$ (number of bubbles per m^3 per μm radius increment) depends only on the average rate of supply of air Q (the volume of air entrained per volume of water per second) with dimensions s^{-1}, ε and radius a, then dimensional consistency implies the scaling law

$$N(a) \propto Q\varepsilon^{-1/3}a^{-10/3} \tag{1}$$

which is consistent with the observed scaling law for bubbles larger than about 1 mm.

The central idea behind turbulent fragmentation[28,29] is that a bubble is likely to break up if the differential pressure forces across the bubble exceed the restoring forces of surface tension. The ratio of these forces is the Weber number, given by

$$\mathrm{We} = (\rho/\gamma)u^2 d \tag{2}$$

where[30] ρ is the fluid density, γ is the fluid surface tension, u is the turbulent velocity field on the scale of the bubble and d is the bubble diameter. The condition for bubble fragmentation is that We exceed a critical value, $\mathrm{We_c}$. Recent experiments suggest that $\mathrm{We_c}$ lies in the range 3–4.7 (refs 30 and 31), and we have used the value $\mathrm{We_c} = 4.7$. An additional constraint is that the bubble undergo shape oscil-

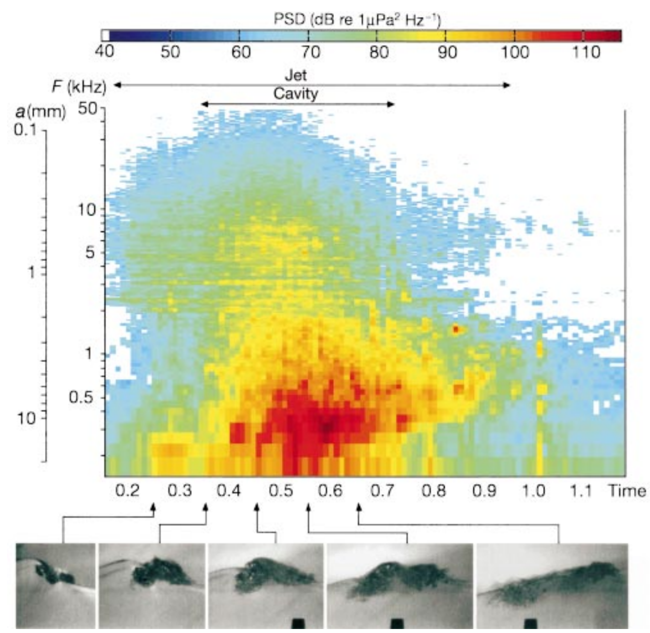

Figure 3 Spectrogram of wave noise calculated from an average of 17 breaking events. This spectrogram is similar to those recorded[37] during the collective oscillations of bubble plumes. The colour contours represent sound intensity plotted on a decibel scale (the intensity is referenced to 1 μPa^2 Hz^{-1}) versus frequency and time. The log scale labelled '*a*' on the left-hand side indicates the radius of a bubble resonant at the corresponding frequency (*F*) on the frequency scale. The two time periods labelled 'Jet' and 'Cavity' are discussed in the text. The wave noise was measured with a hydrophone (International Transducer Corp. 6050c) mounted in the wave flume beneath the bubble plumes. Because the flume is a bounded enclosure, it exhibits acoustic resonances that impose structure on the wave noise spectrum. The amplitude, centre frequencies and spectral widths of the resonant bands were estimated by placing a broad-band acoustic source at the primary plume location and measuring the tank response. These estimates were then used to compensate for the effect of the acoustic resonances on the breaking-wave noise spectrum. The images plotted beneath the spectrogram show the sequence of flow features observed at different times during the acoustic emission. The black bar is 40 mm long.

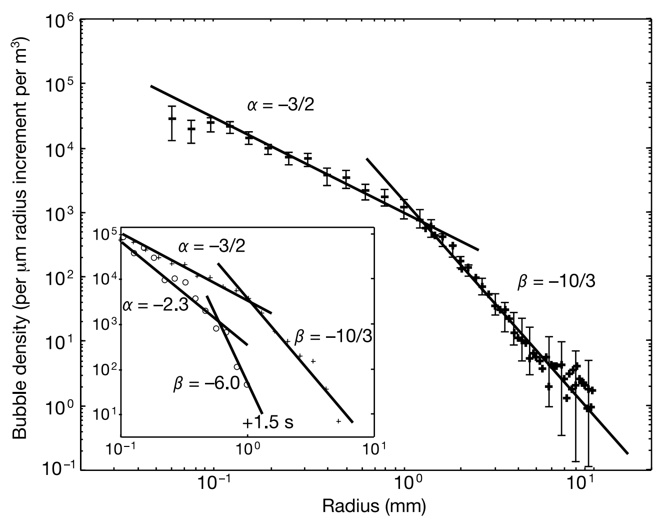

Figure 4 The average bubble size spectrum estimated from 14 breaking events during their acoustic phase. Two camera magnifications were used and the results superimposed to obtain the slightly greater than two decades of bubble radii observed. The vertical scale is number of bubbles per m^3 in a bin radius 1 μm wide. Vertical bars show $\pm$1 s.d. The size distribution shows a marked change in slope at a radius that we are identifying as the Hinze scale. Bubbles larger and smaller than this scale respectively vary as (radius)$^{-10/3}$ and (radius)$^{-3/2}$ denoted by β and α. Inset, the bubble size distribution at the beginning of the quiescent phase (crosses) and 1.5 s into the quiescent phase (open circles). Both slopes of the bubble spectrum have increased noticeably during this time interval. This rapid evolution becomes important when interpreting size distributions collected during the plume quiescent phase.

lations[32] so that the ratio of the bubble major-to-minor axes (the bubble eccentricity) exceeds ~3. This constraint is satisfied if the bubble Reynolds number, given by

$$\mathrm{Re} = ud/\xi \tag{3}$$

where ξ, the fluid kinematic viscosity, is greater than a critical value[32] (~450). If the fluctuating velocity field is assumed to be described by Kolmogorov's inertial subrange, so that $u^2 = 2\varepsilon^{2/3}d^{2/3}$, then only bubbles with radius larger than the Hinze scale

$$a_{\mathrm{H}} = 2^{-8/5}\varepsilon^{-2/5}(\gamma \mathrm{We_c}/\rho)^{3/5} \tag{4}$$

will fragment. The Reynolds number also implies a critical length scale, but the values of γ and ξ for sea water are such that it is smaller than a_{H} for reasonable values of ε. These two scales become comparable only when $\varepsilon \approx 330\,\mathrm{W\,kg^{-1}}$.

In order to test these ideas, we examined sequences of images from breaking waves to identify fragmenting bubbles. Although fragmentation events were frequently observed in the collapsing cavity and shear zone, image sequences of fragmenting bubbles suitable for quantitative analysis were relatively rare: 33 usable events were found in about 25,000 video frames from 125 breaking-wave events. Fragmentation metrics were estimated for each event. The differential velocity across a splitting bubble was estimated by measuring the relative velocity of separation of the fragmentation products, and the bubble eccentricity was measured just before fragmentation. The measured separation velocity was always a factor of 5 or more greater than the expected rise velocity of the bubble products, and buoyancy effects were therefore assumed to be an unimportant source of bias. Figures 5a and 5b show scatter plots of the measured Weber and bubble Reynolds numbers as a function of bubble radius. All the observed fragmenting bubbles were larger than 1 mm in radius, and the estimated Weber and Reynolds numbers were greater than the critical values described above (shown as horizontal lines on the lower portion of the plots). The histogram in Fig. 5c shows the observed bubble eccentricity probability density, and the three images on the right-hand side illustrate the elongation that occurs as a bubble fragments. The observed eccentricity is consistent with the idea that bubbles must reach a critical degree of distortion before they fragment[31].

The turbulent energy dissipation rate inside the fragmenting cavity region can be estimated from equation (4) if the Hinze scale is known. Because bubbles smaller than the Hinze scale are stabilized by surface tension forces, a reasonable estimate for this scale is the radius of the smallest bubbles observed to fragment. This scale estimate differs from that adopted by Garrett *et al.*[18], who used the definition[33] that 95% of the air is contained in bubbles with a radius less than a_{H}. This definition may be more appropriate for steady-state entrainment (for example, steady-state jets), where bubbles have sufficient time to completely fragment. In the present case, these target bubbles are in the process of fragmenting.

The smallest bubbles we observed fragmenting were about 1 mm in radius. An estimate of 1 mm for the Hinze scale is also consistent with the observed change in power-law scaling of the bubble spectrum at around 1 mm (Fig. 4). Taking this to be the Hinze scale, equation (4) yields a value of $\varepsilon = 12\,\mathrm{W\,kg^{-1}}$. The expected Weber and bubble Reynolds numbers as a function of bubble radius for this value of ε calculated from equations (2) and (3) are plotted as solid curves in Fig. 5a and b, and are in good agreement with the observed values. We can also estimate ε from the results of ref. 34, where the normalized dissipation rate per unit length of crest in unsteady breaking waves (Θ) was measured: $\Theta = \varepsilon_1 g/\rho_{\mathrm{w}} C^5$, where ε_1 is the dissipation rate per unit length of crest, g is the acceleration due to gravity, ρ_{w} is the fluid density, and C is the wave speed. These authors measured a value of $\Theta \approx 0.009$ for waves with multiple breaks (like ours). Our measured wave speed was $1.7\,\mathrm{m\,s^{-1}}$, implying a dissipation rate of $\varepsilon_1 = 13.5\,\mathrm{W\,m^{-1}}$. Assuming that all the energy dissipation occurs inside a cylinder 2.5 cm in radius (Fig. 2b) and a void fraction of air within the collapsing region[1] of 0.5, this dissipation rate is equivalent to $\varepsilon = 13\,\mathrm{W\,kg^{-1}}$, which is in good agreement with our dissipation estimate based on the Hinze scale.

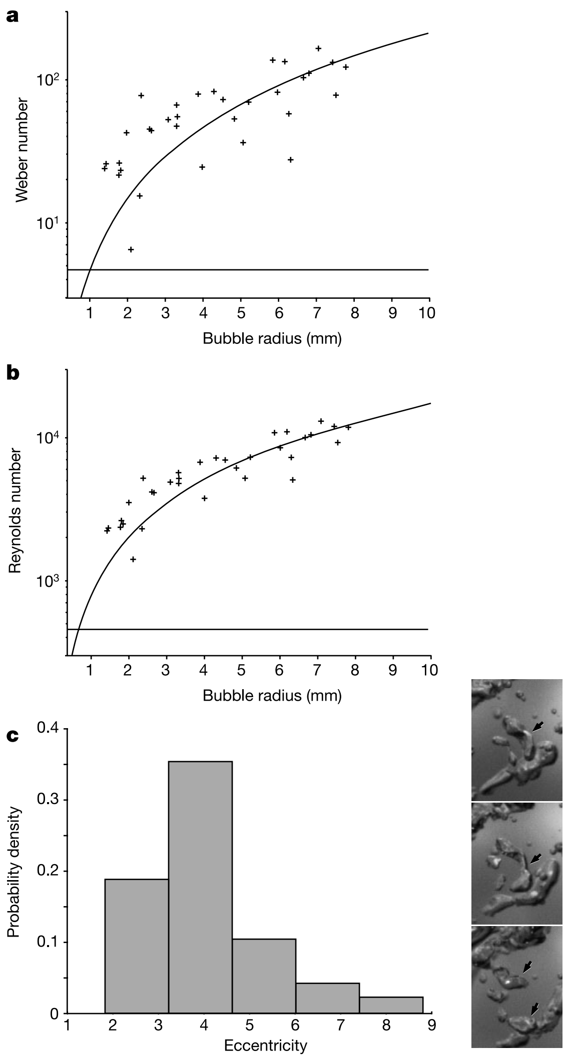

Figure 5 Some bubble fragmentation metrics. Fragmenting bubbles were identified and analysed in image sequences of breaking events. The velocity shear across a splitting bubble was estimated from the separation velocity of the fragmentation products. **a**, The observed Weber number as a function of parent bubble radius. The horizontal line indicates the critical Weber number (4.7) that must be exceeded for fragmentation to occur. The curve shows the theoretical Weber number expected for fully developed turbulence with an energy dissipation rate $\varepsilon = 12\,\mathrm{W\,kg^{-1}}$. **b**, The observed Reynolds number for flow across the parent bubble. The horizontal line shows the critical Reynolds number (~450) that must be exceeded for bubble shape oscillations and elongation, and subsequent fragmentation to occur. The curve shows the expected Reynolds number for the same dissipation rate as above. **c**, The probability density of bubble eccentricity (the ratio of semimajor to semiminor axis) measured just before bubble separation. The mean eccentricity is about 4. Inset, images illustrating the fragmentation of a 4.5-mm-radius bubble in the shear zone of the jet/wave-face interaction region. The arrows in the top two images indicate the fragmentation point, and the two arrows in the bottom image show the fragmentation products.

Bubble entrainment

Large numbers of bubbles smaller than the Hinze scale are entrained, and here we consider their origin. Such bubbles are stabilized by surface tension forces, and do not fragment. Bubbles comparable to the Hinze scale do fragment and produce fragmentation products smaller than the Hinze scale. However, we did not observe any fragmentation products less than $a_H/2$, suggesting they are not a major source of small bubbles. The wave noise spectrogram (Fig. 3) shows that bubbles from around 2 mm radius to bubbles at least as small as 100 μm are created at the start of the active phase, before the cavity fragments, and persist to the end of this phase. The main flow feature associated with these bubbles is the interaction of the plunging jet (including the impact of drops) formed by the overturning wave crest with the wave face (Fig. 2a). The implication is that most bubbles smaller than the Hinze scale are formed by the jet/wave-face interaction throughout the active phase.

There is a significant body of literature describing air entrainment by steady-state, laminar and turbulent plunging jets[19–21]. Although jet entrainment in breaking waves is by transient, inclined jets moving relative to the water surface, it is possible to derive a power scaling law for the bubble spectrum from the mechanics of steady-state jets. Following dimensional arguments similar to those used by Garrett *et al.*[18] to derive their scaling law for turbulent fragmentation, we will assume that the bubble spectral level is a multiplicative function of γ, ρ, a and jet velocity ν. Surface tension (γ) is included because we are considering bubbles smaller than the Hinze scale where surface tension effects are assumed to be important. The jet velocity is included to account for the fact that low-velocity jet air entrainment rates are known to scale[19] with ν^2. For dimensional consistency, the bubble size spectrum must then scale as:

$$N(a) \propto Q(\gamma/\rho)^{-3/2}\nu^2 a^{-3/2} \qquad (5)$$

Although we do not have a mechanistic argument supporting equation (5), the $-3/2$ power scaling law for bubble spectral density with bubble radius is in good agreement with the observed spectral slope for bubbles smaller than the a_H. A greater understanding of the deterministic entrainment physics would require the kind of detailed analysis presented by, for example, ref. 21 for bubble entrainment by single drop impacts.

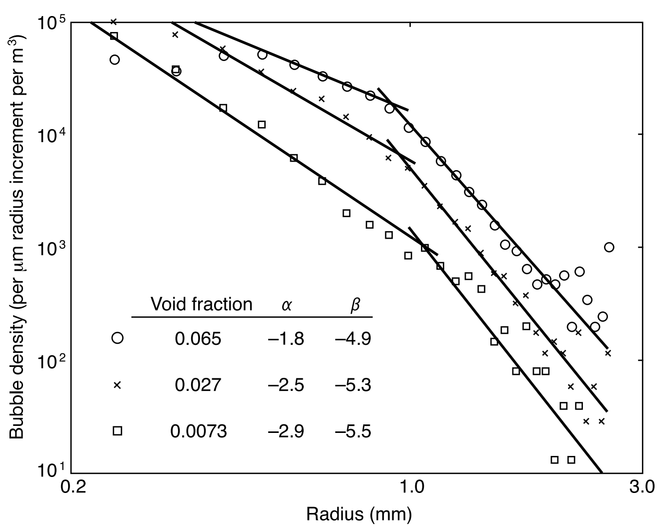

Figure 6 Oceanic bubble size distributions observed 30 cm below whitecaps during the plume quiescent phase. Each curve was obtained by analysing multiple images from a single breaking event. The exact time after the beginning of the quiescent phase is unknown, but is of the order of a second. Using the void fraction of air as a surrogate for plume age, the size distribution slopes α and β can be seen to increase with increasing plume age as bubbles are lost to the imaging volume through the effects of buoyant degassing and dissolution.

Oceanic waves

The main interest in bubble size spectra beneath breaking waves is their relevance to oceanic phenomena, such as air–sea gas exchange. It is important, then, to consider the relationship between our laboratory results and air entrainment processes occurring in open-ocean waves where different routes to breaking exist, and different wave amplitudes and frequencies are encountered.

Ideally, an analysis of bubble formation mechanisms in oceanic waves would be based on visual images of the flow features occurring inside whitecaps and measurements of bubble fragmentation and entrainment. However, the best observations of open-ocean whitecaps available at present are oceanic bubble spectra from spilling breakers collected a second or so into the quiescent plume phase approximately 30 cm beneath the surface[14]. Despite this limitation, we can make some inferences by comparing the oceanic bubble spectra with those observed in the laboratory.

Figure 6 shows typical bubble size spectra from three separate breaking events observed off the coast of Southern California during the winter of 2000. The wind speed, significant wave height, wave period and water temperature were respectively 7–10 m s^{-1}, 2.5–3.5 m, 9–12 s and 13.2 °C. The bubble spectra from the interiors of whitecap plumes were observed using an optical bubble counting instrument[26] mounted on a surface-tracking frame deployed from the research platform FLIP. It was impossible to determine the exact end of the active phase during the breaking events and so the quiescent plume age cannot be determined precisely, but is of the order of 1 s. Underwater video footage of oceanic whitecaps and our flume study show that the plume has well-defined spatial boundaries at the end of the active phase. As a first approximation, the effect of spatial heterogeneity on void fraction can be neglected, and relative plume age can be determined using void fraction of air as a surrogate for time into the quiescent phase[1]. Under this assumption, plume age increases from the top to the bottom of the figure.

The most revealing aspect of the oceanic spectra is that, like the flume spectra, they exhibit two power-law scales and an increase in slope at around 1 mm bubble radius. This change in slope has also been observed in quiescent plume size distributions measured beneath breaking surf[35]. The existence of a break-point in the oceanic spectra so similar to that observed in the laboratory suggests that the Hinze scale also exists in the open ocean where spilling breakers predominate. This oceanic Hinze scale is evidence that, as with the laboratory waves, turbulent fragmentation drives the large end of the bubble spectrum.

Although the open-ocean whitecaps and breaking surf were different from the laboratory waves in terms of amplitude, frequency and breaker type, they have similar Hinze scales. There are reasons to expect that this would be the case. Measurements[34] show that dissipation rates remain relatively constant for multiple break events over a range of integral wave slopes and, from equation (4), the Hinze scale shows a relatively weak dependence on the turbulent dissipation rate. A change in dissipation rate from 3 to 30 W kg^{-1} corresponds to a change in Hinze scale from 1.7 to 0.7 mm.

The second revealing aspect of the oceanic spectra is their power-law scaling. We would expect to observe $\alpha = -3/2$ and $\beta = -10/3$ for bubble spectra measured at the end of the active phase, and slopes greater than these for older plumes (Fig. 4 inset). In fact, we do observe similar, but somewhat greater slopes, and plumes with increasing age (inferred using their void fraction) show increasing slopes with increasing time.

The importance of the Hinze scale

We have presented qualitative and quantitative experimental evidence that two primary mechanisms control the numbers and sizes of bubbles created by laboratory and oceanic breaking waves. The physical mechanisms operate on different regions of the bubble size spectrum, separated by the Hinze scale. Bubbles larger than the

Hinze scale are subject to fragmentation by turbulent and sheared flow, and show a $-10/3$ power-law scaling with radius. Bubbles smaller than the Hinze scale are stabilized by surface tension, and show a $-3/2$ power-law scaling with radius. The $-10/3$ power law scaling is consistent with recent theoretical predictions made by Garrett *et al.*[18], and the $-3/2$ power law scaling is consistent with a dimensional analysis of jet entrainment presented here.

Despite the fact that breaking in the open ocean is predominately spilling, rather than plunging, a comparison of open-ocean spectra with those observed in the laboratory show important similarities. There is clear evidence of a Hinze scale in the oceanic bubble spectra, and spectral slopes are consistent with the evolving slopes of quiescent plumes. The fact that we see the Hinze scale in both open-ocean and surf-zone spectra, arising from spilling and plunging breakers with very different scales, implies that the same bubble formation mechanisms are operating in each of these environments. This conclusion is supported by the spectral slopes observed in quiescent oceanic plumes, which are similar to, but somewhat greater than, the slopes observed at the end of the active phase in the laboratory. This increase in slope with increasing time is expected, as bubbles are lost through buoyant degassing and become smaller as they dissolve. We also note that Loewen *et al.*[36] have measured bubble spectra immediately behind the crests of gently spilling laboratory waves. The slope of their distribution for bubbles larger than 1 mm are similar to our flume and open-ocean results, supporting the argument that the mechanism that creates large bubbles is the same beneath spilling and plunging breakers.

The existence of simple scaling laws for bubble number density separated by a length scale that depends only on the turbulent dissipation rate has important implications for modelling turbulent, two-phase flow in a wide variety of natural and man-made systems, including modelling the bubble-mediated transfer of greenhouse gases and aerosol production, both important for global climate change, and models of wave-induced oceanic ambient noise. □

Received 15 May; accepted 4 July 2002; doi:10.1038/nature00967.

1. Lamarre, E. & Melville, W. K. Air entrainment and dissipation in breaking waves. *Nature* **351,** 469–472 (1991).
2. Wallace, D. W. R. & Wirick, C. D. Large air–sea fluxes associated with breaking waves. *Nature* **356,** 694–696 (1992).
3. Farmer, D. M., McNeil, C. L. & Johnson, B. D. Evidence for the importance of bubbles in increasing air–sea gas flux. *Nature* **361,** 620–623 (1993).
4. Melville, W. K. The role of surface-wave breaking in air-sea interaction. *Annu. Rev. Fluid. Mech.* **28,** 279–321 (1996).
5. Thorpe, S. A. The effect of Langmuir circulation on the distribution of submerged bubbles caused by breaking wind waves. *J. Fluid. Mech.* **142,** 151–170 (1984).
6. Medwin, H. & Breitz, N. D. Ambient and transient bubble spectral densities in quiescent seas and under spilling breakers. *J. Geophys. Res.* **94,** 12751–12759 (1989).
7. Hwang, P. A., Hsu, Y. L. & Wu, J. Temperature effects on generation and entrainment of bubbles induced by a water jet. *J. Phys. Oceanogr.* **20,** 19–28 (1990).
8. Monahan, E. C. & Lu, M. Acoustically relevant bubble assemblages and their dependence on meteorological parameters. *IEEE J. Ocean. Eng.* **15,** 340–349 (1990).
9. Thorpe, S. A. Bubble clouds and the dynamics of the upper ocean. *Q. J. R. Meteorol. Soc.* **118,** 1–22 (1992).
10. Thorpe, S. A., Bowyer, P. & Woolf, D. K. Some factors affecting the size distributions of oceanic bubbles. *J. Phys. Oceanogr.* **22,** 382–389 (1992).
11. Farmer, D. & Li, M. Patterns of bubble clouds organized by Langmuir circulation. *J. Phys. Oceanogr.* **25,** 1426–1440 (1995).
12. Bezzabotnov, V. S., Bortkovskiy, R. S. & Timanovskiy, D. F. On the structure of the two-phase medium generated at wind-wave breaking. *Izvest. Atmos. Ocean. Phys.* **22,** 922–928 (1986).
13. Deane, G. B. & Stokes, M. D. Air entrainment processes and bubble size distributions in the surf zone. *J. Phys. Oceanogr.* **29,** 1393–1403 (1998).
14. Stokes, M. D., Deane, G. B., Vagle, S. & Farmer, D. in *Gas Transfer at Water Surfaces* Geophysical Monographs 127 (eds Donelan, M. A., Drennan, W. M., Saltzman, E. S. & Wanninkhof, R.) 278–285 (American Geophysical Union, Washington, DC, 2002).
15. de Leeuw, G. D. & Cohen, L. H. in *Gas Transfer at Water Surfaces* Geophysical Monographs 127 (eds Donelan, M. A., Drennan, W. M., Saltzman, E. S. & Wanninkhof, R.) 271–277, (American Geophysical Union, Washington, DC, 2002).
16. Longuet-Higgins, M. S. The crushing of air cavities in a liquid. *Proc. R. Soc. Lond. A* **439,** 611–626 (1992).
17. Baldy, S. A generation-dispersion model of ambient and transient bubbles in the close vicinity of breaking waves. *J. Geophys. Res.* **98,** 18277–18293 (1993).
18. Garrett, C., Li, M. & Farmer, D. The connection between bubble size spectra and energy dissipation rates in the upper ocean. *J. Phys. Oceanogr.* **30,** 2163–2171 (2000).
19. Van De Sande, E. & Smith, J. M. Jet break-up and air entrainment by low velocity turbulent water jets. *Chem. Eng. Sci.* **31,** 219–224 (1976).
20. Bonetto, F. & Lahey, R. T. Jr An experimental study on air carryunder due to a plunging jet. *Int. J. Multiphase Flow* **19,** 281–294 (1993).
21. Pumphrey, H. C. & Elmore, P. A. The entrainment of bubbles by drop impacts. *J. Fluid Mech.* **220,** 539–567 (1990).
22. Koga, M. Bubble entrainment in breaking wind waves. *Tellus* **34,** 481–489 (1982).
23. Loewen, M. R., O'Dor, M. A. & Skafel, M. G. Bubbles entrained by mechanically generated breaking waves. *J. Geophys. Res.* **101,** 20759–20820 (1996).
24. Bonmarin, P. Geometric properties of deep water breaking waves. *J. Fluid Mech.* **209,** 405–433 (1989).
25. Minnaert, M. On musical air bubbles and the sounds of running water. *Phil. Mag.* **16,** 235–248 (1933).
26. Leighton, T. G. *The Acoustic Bubble* (Academic, San Diego, 1994).
27. Stokes, M. D. & Deane, G. B. A new optical instrument for the study of breaking waves at high void fractions within breaking waves. *IEEE J. Ocean. Eng.* **24,** 300–311 (1999).
28. Kolomogorov, A. N. O droblenii kapel' v turbulentnom potoke. *Dokl. Acad. Nauk USSR* **66,** 825–828 (1949).
29. Hinze, J. O. Fundamentals of the hydrodynamic mechanism of slitting in dispersion processes. *J. Am. Inst. Chem. Eng.* **1,** 289–295 (1955).
30. Lewis, D. A. & Davidson, J. F. Bubble splitting in shear flow. *Trans. Inst. Chem. Eng.* **60,** 283–291 (1982).
31. Martínez-Bazán, C., Montañés, J. L. & Lasheras, J. C. On the breakup of an air bubble injected into a fully developed turbulent flow. I. Breakup frequency. *J. Fluid Mech.* **401,** 157–182 (1999).
32. Fan, L.-S. & Tsuchiya, K. *Bubble Wake Dynamics in Liquids and Liquid-Solid Suspensions* (Butterworth-Heinemann, Boston, 1990).
33. Clay, P. H. The mechanism of emulsion formation in turbulent flow: theoretical part and discussion. *Proc. R. Acad. Sci.* **43,** 979–990 (1940).
34. Loewen, M. R. & Melville, W. K. Microwave backscatter and acoustic radiation from breaking waves. *J. Fluid Mech.* **224,** 601–623 (1991).
35. Deane, G. B. Sound generation and air entrainment by breaking waves in the surf zone. *J. Acoust. Soc. Am.* **102,** 2671–2689 (1997).
36. Loewen, M. R., O'Dor, M. A. & Skafel, M. G. in *Third Int. Symp. on Air-Water Gas Transfer* (eds Jahne, B. & Monahan, E. C.) 337–349 (AEON Verlag & Studio, Hanau, Germany, 1995).
37. Loewen, M. R. & Melville, W. K. An experimental investigation of the collective oscillations of bubble plumes entrained by breaking waves. *J. Acoust. Soc. Am.* **95,** 1329–1343 (1992).

Acknowledgements

We thank G. Devine and J. Uyloan for assistance in laboratory data analysis, and the crew of RP *FLIP* during oceanic deployments. We also thank D. Farmer, M. Li and C. Garrett for discussions. This work was supported by the National Science Foundation and the Office of Naval Research.

Competing interests statement

The authors declare that they have no competing financial interests.

Correspondence and requests for materials should be addressed to G.B.D. (e-mail: grant@mpl.ucsd.edu).

